ACS OMEGA

http://pubs.acs.org/journal/acsodf

Article

Study of a High-Index Dielectric Non-Hermitian Metasurface and Its Application in Holograms

Xiangrong Wu, Jiaxi Zhu, Feng Lin,* Zheyu Fang,* and Xing Zhu

Cite This: *ACS Omega* 2022, 7, 44743−44749

Read Online

ABSTRACT: We demonstrate that a high-index dielectric Si metasurface with a designed chiral unit structure possesses an exceptional point (EP) when it is described by a non-Hermitian Hamiltonian associated with the transmission matrix. By encircling any path in the parameter space around the EP, topologically protected 2π-phase accumulation occurs. These typical non-Hermitian properties are ascribed to complex scattering phenomena related to the coupling between electric and magnetic dipolar modes from the high-index dielectric Si metasurface. The topologically guaranteed entire 2π-phase accumulation and chiral distinction around the EP open up many promising possibilities in nanophotonic device designing; for instance, phase-only and polarization multiplexing holograms are realized in this work.

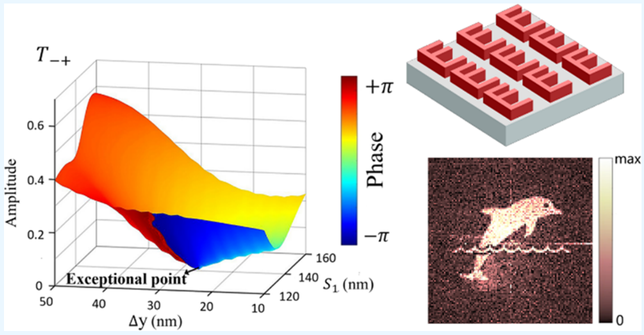

1. INTRODUCTION

Metasurfaces, periodic arrangements of artificial subwavelength antennas with different shapes and sizes,[1−7] have better optical performances than conventional optical counterparts. Up to now, nano-optical devices based on metasurfaces have been widely used in holograms,[8−12] wave plates,[13−15] metalenses,[16−19] and so on. From a fundamental perspective, these constituent subwavelength antennas, which are treated as optical multipolar resonators and thereby subject to radiative loss or dissipation under illumination, can be described by an open system of non-Hermitian Hamiltonians.[20−25] In recent years, quite a lot of works have demonstrated that some non-Hermitian systems possess passive parity-time (PT) symmetry, though in the absence of optical gain, and present different optical behaviors from Hermitian systems. For example, eigenvectors of a non-Hermitian Hamiltonian do not require to be orthogonal, and at certain points in the parameter space called exceptional points (EPs), two eigenvectors, as well as their eigenvalues, coalesce. Metasurfaces provide an excellent arena for exploring the underlying physics of non-Hermitian systems because they can be engineered with precise control over the structural parameters that govern resonator properties and easily be measured by standard optical reflection or transmission.[26−30] Recently, PT-symmetric metasurfaces and their topological features of non-Hermitian matrices near EPs have been investigated;[31−3531−35] for example, Genevet et al. demonstrated that by precisely designing the sizes of Al nanoantennas, a planar chiral plasmonic metasurface exhibits 2π topological phase accumulation distributed along any arbitrarily closed parameter loop encircling the EP in a reflection regime.[36] Up to now, however, most of the works have focused on plasmonic metasurfaces, wherein the phenomena related to non-Hermitian properties such as anomalous transparency,[37] unidirectional transmission,[38−41] power oscillation,[42,43] and so on mainly arise from electric dipolar scattering and decaying of metallic nanoantennas, completely irrespective of other orders of resonant modes.

In this work, we propose a high-index dielectric Si metasurface that displays a chiral shape of "E" and introduces the coupling between electric and magnetic dipolar modes. The light transmission through the metasurface can be well described by a non-Hermitian Hamiltonian, which presents spontaneous PT-symmetry breaking in the parameter space. In particular, the EP is associated with the structural chirality of the metasurface, and topologically protected 2π-phase accumulation occurs by encircling any path around the EP. These properties can be exploited in phase-only and polarization multiplexing holograms.

2. RESULTS AND DISCUSSION

As schematically shown in Figure 1a,b, a unit cell of our designed high-index dielectric (here, taken as Si) metasurface contains

Received: July 14, 2022
Accepted: November 4, 2022
Published: December 2, 2022

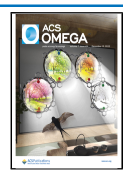

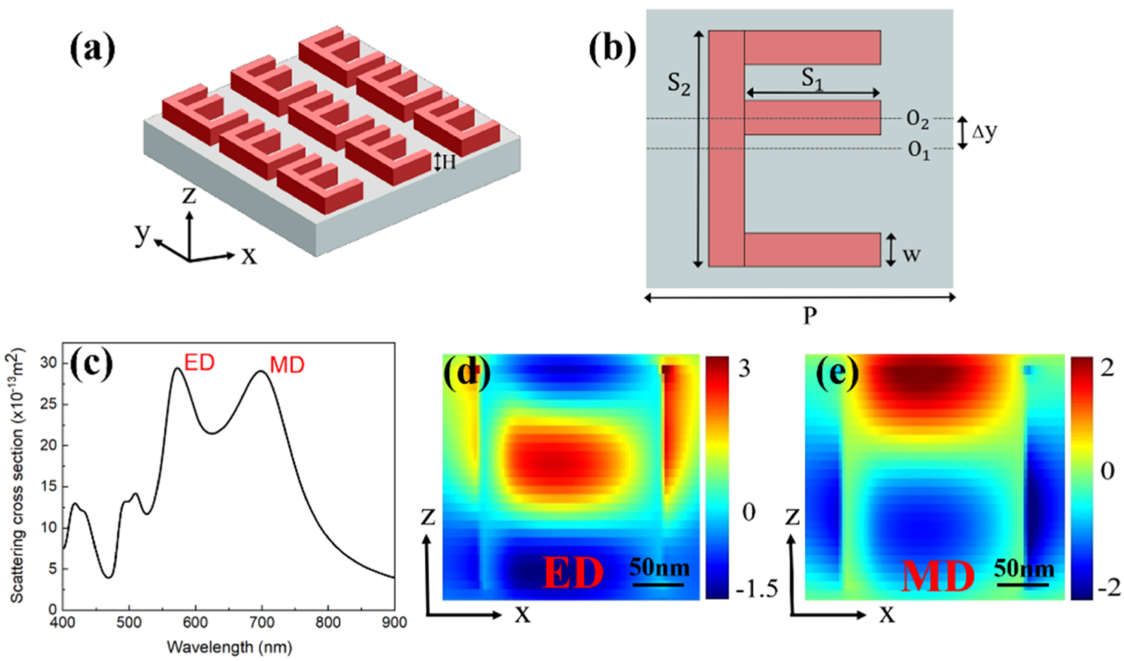

Figure 1. (a) Schematic of a high-index Si metasurface on a glass substrate in a perspective view, which is made up of arrays with "E" shape structures. (b) Top view of a unit cell, which contains three parallel separate boards and another one orthogonally contacts them. In our simulation, the fixed geometrical parameters are $H = 250$ nm, $P = 250$ nm, $S_2 = 210$ nm, and $w = 30$ nm, and the varied parameters are S_1, which is the length of the three parallel boards, and Δy, which is the deviation from the central dash line O_1 to the middle board line O_2 in the y-direction. (c) Scattering cross section of the "E" structure, where $S\_1 = 180$ nm and $\Delta y = 25$ nm. (d, e) Electric field (Ex) distribution of ED and MD of the middle board on the x−z plane, respectively.

three parallel separate boards in subwavelength sizes, and another one orthogonally contacts them on the side, displaying a shape of "E" from the top view (Figure 1b), which is a characteristic of planar chirality. The specific geometric parameters are labeled in Figure 1a,b. The whole metasurface is composed of two-dimensional (2D) arrays of "E" structures with a period of 250 nm in the x- and y- directions. The high-index dielectric metasurface is favorable to enhance light−matter interaction in the nanoscale, generating resonance-based multipole and multimode optical responses. Here, the scattering properties of the middle board within the individual "E" structure were calculated by commercial finite-difference time-domain software (Lumerical FDTD). The refractive index of Si was taken from Palik's book.[44] The index of the surrounding medium was taken to be 1. From the calculated scattering spectrum shown in Figure 1c, two main resonance peaks appear at wavelengths of 573 and 700 nm, which correspond to electric dipole (ED) and magnetic dipole (MD) modes, respectively. These modes are clearly identified by their characteristic distribution of electromagnetic fields at the respective resonance positions,[45] as shown in Figure 1d,e, where the Ex field distribution is taken from the x−z plane of the central board. Note that the other three boards are also dominated by the two modes; the intensity and wavelength position of ED and MD modes slightly vary on changing the geometrical parameters of the "E" structure.

In consideration of the ED and MD being subject to radiative loss or dissipation under light illumination, the "E" structure thus would be well described by non-Hermitian Hamiltonians. The ED is expressed as $\vec{p} = \tilde{p}\, e^{j\omega t}$, and MD is expressed as $\vec{m} = \tilde{m}\, e^{j\omega t}$, which couple strongly to the incident radiation field $\vec{E}_i = (E_{ix}, E_{iy})e^{j\omega t}$. In a rough approximation, $\vec{p}$ is dominated by p_x, and $\vec{m}$ is dominated by m_y, which are orthogonal mutually. The dipole moments are related to the incident electric field through the polarizability matrix as follows

$$\begin{pmatrix} \delta_x - j\gamma_x & -\kappa \\ -\kappa & \delta_y - j\gamma_y \end{pmatrix}\begin{pmatrix} p_x \\ m_y \end{pmatrix} = \begin{pmatrix} g_x E_{ix} \\ g_y E_{iy} \end{pmatrix} \tag{1}$$

where $\delta_{x,y}$ are the frequencies detuning from the resonances of ED and MD, respectively, $\gamma_{x,y}$ are the damping rates of the two dipoles, respectively, κ is the coupling strength between the two dipoles, and $g_{x,y}$ are the coupling factors between the incident field and the two dipoles, respectively. For clarity, we define $\Omega = \begin{pmatrix} \delta_x - j\gamma_x & -\kappa \\ -\kappa & \delta_y - j\gamma_y \end{pmatrix}$ in the following. The transmitted field is the superposition of the incident field and the scattered fields of the two dipoles, expressed in the linear polarization bases x- and y-directions as

$$\begin{aligned} \vec{E}_{out} &= T_{lin}\vec{E}_{in} = \begin{pmatrix} T_{xx} & T_{xy} \\ T_{yx} & T_{yy} \end{pmatrix}\vec{E}_{in} \\ &= Q\begin{pmatrix} g_x^2(\delta_y - j\gamma_y) & g_x g_y \kappa \\ g_x g_y \kappa & g_y^2(\delta_x - j\gamma_x) \end{pmatrix}\begin{pmatrix} E_{ix} \\ E_{iy} \end{pmatrix} + I\begin{pmatrix} E_{ix} \\ E_{iy} \end{pmatrix} \end{aligned} \tag{2}$$

where $Q = \frac{i\omega\eta_0}{2p^2}\frac{1}{\det(\Omega)}$, and I is the unit matrix. The transmission matrix then takes the form

$$T_{lin} = Q\begin{pmatrix} g_x^2(\delta_y - j\gamma_y) & g_x g_y \kappa \\ g_x g_y \kappa & g_y^2(\delta_x - j\gamma_x) \end{pmatrix} + I \tag{3}$$

https://doi.org/10.1021/acsomega.2c04448
ACS Omega 2022, 7, 44743−44749

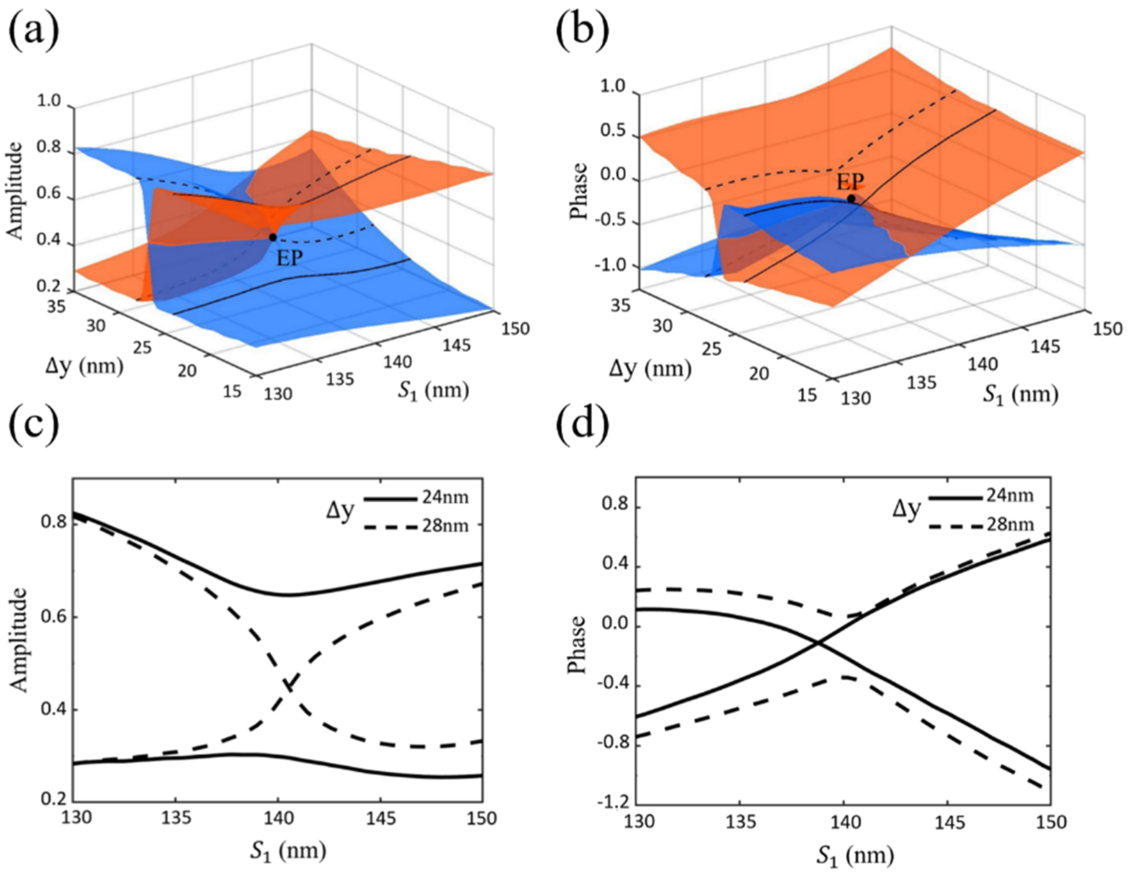

Figure 2. Eigenvalues near the EP on the self-intersecting Riemann surfaces. (a) Amplitude and (b) phase of two eigenvalues at $\lambda = 550$ nm in $\boldsymbol{R} = (S_1, \Delta y)$ parameter space. The orange and blue pieces correspond to the two eigenvalues. The EP is indicated by black dots, where the corresponding parameters are $(S_1, \Delta y) = (141$ nm, 26 nm). For the given values of Δy, the intersection behaviors with the amplitude and phase of the eigenvalues are opposite. When the value of Δy is fixed, (c) amplitude and (d) phase of the eigenvalues are as the function of parameter S_1. The solid and dashed lines represent $\Delta y = 24$ nm and $\Delta y = 28$ nm, respectively.

and its eigenvalues are

$$\lambda_{\pm} = 1 + \frac{Q}{2}[g_x^2(\delta_y - j\gamma_y) + g_y^2(\delta_x - j\gamma_x) \pm \sqrt{\Delta}] \tag{4}$$

where

$$\Delta = 4g_x^2 g_y^2 \kappa^2 - [g_y^2(\gamma_x + j\delta_x) - g_x^2(\gamma_y + j\delta_y)]^2 \tag{5}$$

When $\Delta = 0$, the eigenvalues as well as the eigenstates coalesce, implying the occurrence of an EP.

For the high-index metasurface, $T_{xx} \neq T_{yy}$ due to the planar chiral anisotropy, and $T_{xy} = T_{yx}$ due to the approximate optical reciprocity arising from mirror symmetry across the plane of the metasurface. Taking into account the mentioned properties of the components of T_{lin}, it is more straightforward to re-express the transmission matrix in the circular polarization basis as

$$T_{\text{cir}} = \begin{bmatrix} T_{++} & T_{+-} \\ T_{-+} & T_{--} \end{bmatrix} = \frac{1}{2}\begin{bmatrix} (T_{xx} + t_{yy}) + j(T_{xy} - T_{yx}) & (T_{xx} - T_{yy}) - j(T_{xy} + T_{yx}) \\ (T_{xx} - T_{yy}) + j(T_{xy} + T_{yx}) & (T_{xx} + T_{yy}) - j(T_{xy} - T_{yx}) \end{bmatrix} \tag{6}$$

where subscripts + and − represent left circularly polarized (LCP) and right circularly polarized (RCP), respectively. It can be seen from the transmission matrix that $T_{++} = T_{--}$, and the eigenvalue are $t_{\pm} = T_{++} \pm \sqrt{T_{+-}T_{-+}}$. The condition required to achieve EP is

$$T_{+-}T_{-+} = 0 \tag{7}$$

By comparing eqs 5 and 6, it is found that

$$\Delta = 4\frac{1}{Q^2}T_{+-}T_{-+} \tag{8}$$

which is in agreement with condition 7. Considering the ED and MD modes occurring in the "E" structures, we can adjust the electric and magnetic resonances with respect to each other by a variation of the "E" structural parameters, in consequence, allow for engineering the transmission behaviors, and thus arrive at condition 7, i.e., $T_{+-} = 0$ or $T_{-+} = 0$.

The eigenvalues and eigenstates of the transmission matrix (eq 6) can be solved as a function of geometrical parameters that was defined as a parameter space $\boldsymbol{R} = (S_1, \Delta y)$. The chosen parameters can more effectively tune the loss and coupling of the ED and MD, so the EP can be achieved at the appropriate parameter values when the requirement of $T_{+-} = 0$ or $T_{-+} = 0$ is satisfied. The amplitude and phase of the eigenvalues of the transmission matrix are presented in Figure 2a,b, respectively. It is found that the EP is located at the point of intersection (S_1 =

https://doi.org/10.1021/acsomega.2c04448
ACS Omega 2022, 7, 44743−44749

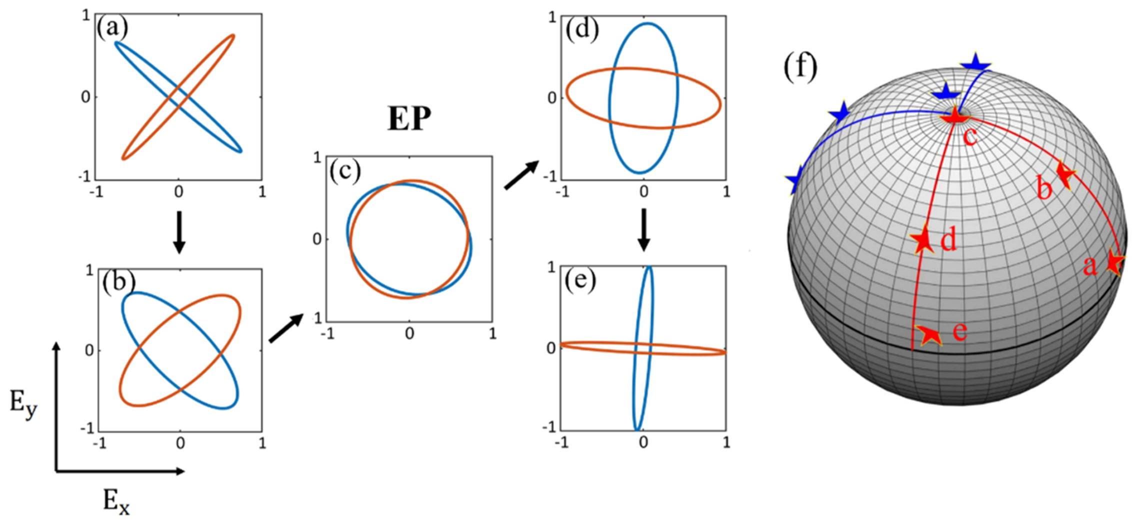

Figure 3. Evolution of polarization eigenstates of the transmission matrix by changing S_1. With the same $\Delta y = 26$ nm, (a) $S_1 = 122$ nm, (b) $S_1 = 134$ nm, (c) $S_1 = 141$ nm, (d) $S_1 = 147$ nm, and (e) $S_1 = 174$ nm. (f) Polarization eigenstates for different parameters plotted on the Poincaré sphere with LCP at the north pole.

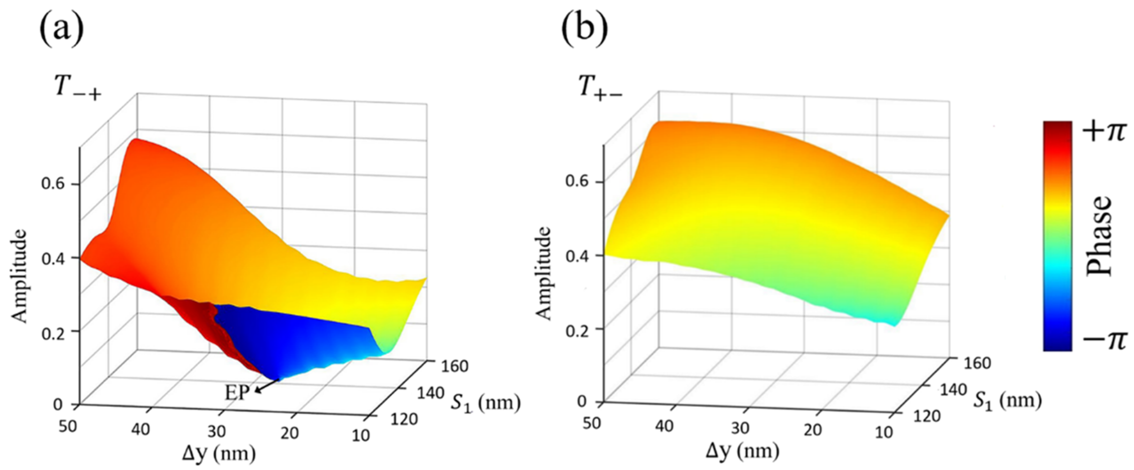

Figure 4. Amplitude and phase of circular polarization conversion coefficients of the transmission matrix. (a) T_{-+} and (b) T_{+-} in the parameter space in the range of $S_1 \in [120, 160$ nm$]$ and $\Delta y \in [10, 50$ nm$]$. An EP appears at $(S_1, \Delta y) = (141$ nm, 26 nm$)$ in T_{-+}. The color bar in the figure represents the phase of the transmission coefficient. The vortex phase distribution and topological protected 2π-phase accumulation of T_{-+} can be found by wrapping around the EP.

141 nm, Δy = 26 nm) on a self-intersecting Riemann sheet, which means that the real and imaginary parts of two eigenvalues degenerate into a point. Very clearly, the eigenvalues will not return to their original values under one full loop around the EP but will rather be swapped, and they will return to their original values only under two full loops. This is direct and strong evidence for proving the existence of the EP. For a closer look, cut from Figure 2a,b, we checked the different behaviors of eigenvalues with S_1 at the fixed $\Delta y = 24$ and 28 nm (Figure 2c,d), respectively. Taking the "E" structure into account, the variation of Δy implies that the near-field coupling between the subwavelength boards is to be varied. Δy = 24 nm represents weak coupling and Δy = 28 nm represents strong coupling. The amplitude of eigenvalues undergoes an anticrossing behavior at Δy = 24 nm with S_1, while crossing at Δy = 28 nm. The phase of eigenvalues has exactly the opposite processes, which undergoes a crossing behavior at Δy = 24 nm, while anticrossing at Δy = 28 nm. This intersecting behavior is a unique feature of self-intersecting Riemann surfaces, which fully follows the intrinsic topology of non-Hermitian systems. These characteristics strongly confirm that the EP is located at 24 nm < Δy^{EP} < 28 nm.

The eigenstates of the transmission matrix are two corotating polarization ellipses, which display different ellipticities and orientation angles determined by the chosen parameters. Here, Δy was set to be 26 nm, and the evolution of polarization eigenstates of the transmission matrix with S_1 is shown in Figure 3a−e. At S_1 = 122 and 134 nm, the relative loss of the system is small, so $\gamma < 2\kappa$ (here, $g_x = g_y$, $\delta_x = \delta_y$, $\gamma = |\gamma_x - \gamma_y|$), corresponding to the PT-symmetric state. The polarization eigenstates show that the angles between the major axis and the y-axis are $\pm 45°$ (Figure 3a,b). For S_1 = 141 nm and $\gamma = 2\kappa$, the coalescence of the eigenstates from two polarization ellipses into one circular polarization roughly emerges, implying the occurrence of the degenerate of the eigenstates. Unlike the Hermitian system, eigenstates are no longer described by a complete basis, and the eigenspace is defective, where the two degenerate polarization eigenstates are left circularly polarized (LCP), indicating that despite the absence of rotational symmetry, LCP light transmits through the high-index dielectric metasurface without any

https://doi.org/10.1021/acsomega.2c04448
ACS Omega 2022, 7, 44743−44749

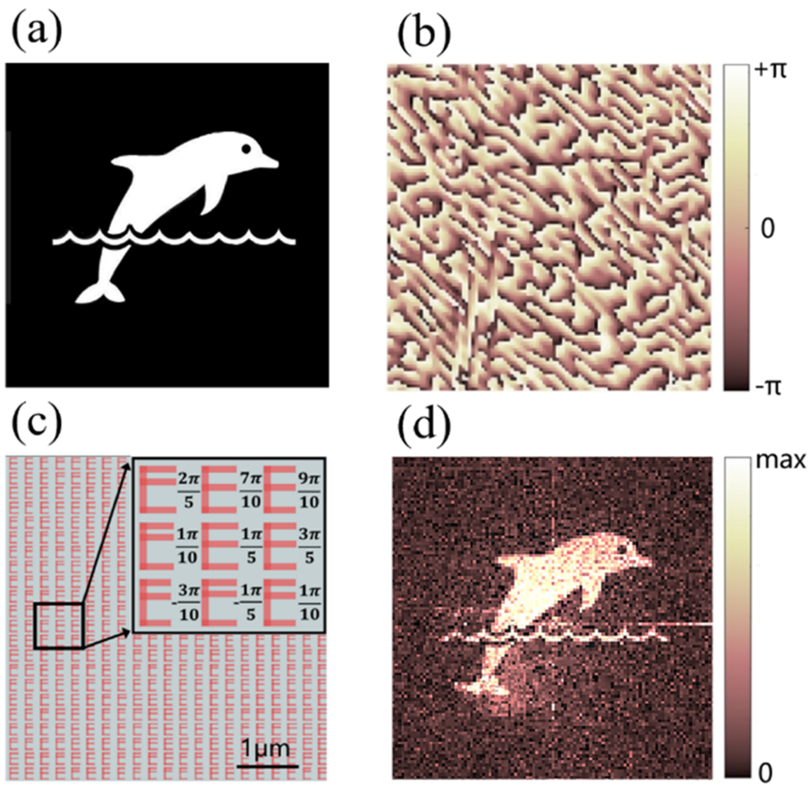

Figure 5. Simulation and design of the phase-only high-index metasurface hologram. (a) The preset image for the 2D hologram. (b) Phase distribution of the hologram with 100 pixels × 100 pixels. (c) The "E" structure program of partial metasurface that implements the phase distribution of (b). The inset shows the magnified "E" structures and the corresponding phase for each unit. (d) The transmission hologram under LCP incidence at $\lambda = 550$ nm.

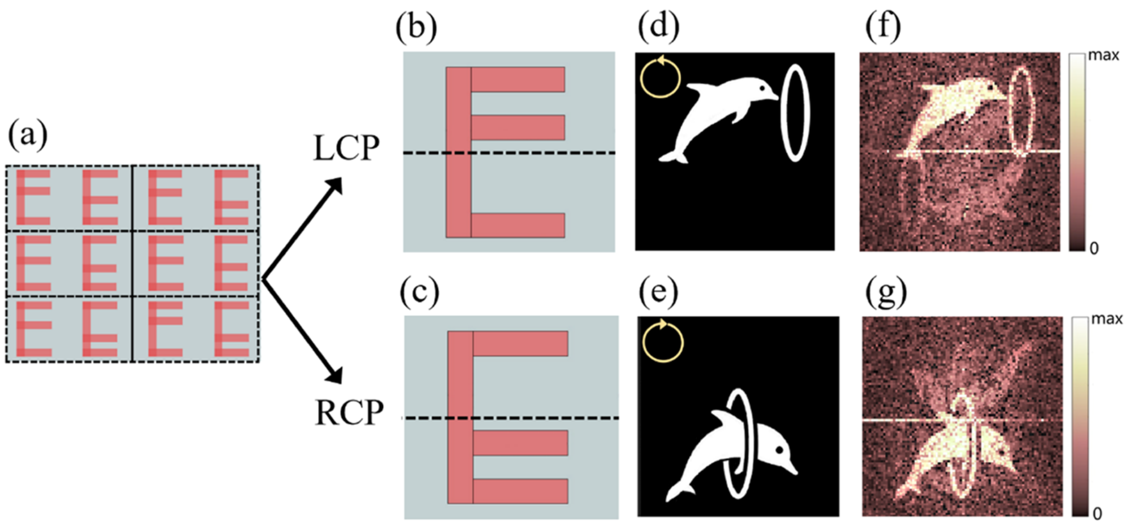

Figure 6. Design and simulation of the polarization multiplexing high-index metasurface hologram. (a) A designed metasurface hologram in which two distinct chiralities of the "E" structures are contained within a unit. (b) For $\Delta y > 0$, the 2π-phase accumulation holds for the LCP. (c) For $\Delta y < 0$, the 2π-phase accumulation holds for the RCP. (d, e) Two target images under different chirality incident lights. (f) Under LCP incidence, the holographic image is "dolphin1". (g) Under RCP incidence, the holographic image is "dolphin2". The incident wavelength is $\lambda = 550$ nm.

conversion to right circular polarization (RCP; Figure 3c). At S_1 = 147 and 174 nm, the relative loss increases, which means $\gamma > 2\kappa$, known as a PT-symmetric breaking state. These polarization eigenstates are still corotating polarization ellipses, whereas the angles between the major axis and the y-axis are 0 and 90°, respectively (Figure 3d,e). The eigenstates are represented on the Poincaré sphere (Figure 3f), and it can be seen that although the spatial symmetry of the transmission matrix remains unchanged, the PT-symmetry breaking results in a sudden 45° rotation of the azimuth.

Figure 4a shows the amplitude and phase of the transmission matrix element T_{-+}, which also denotes the circular polarization conversion coefficient as functions of S_1 and Δy. As expected, the transmission matrix from the metasurface can be tailored with varying parameters, due to the scattering variation of the ED and MD arising from the "E" structures. Following the analysis of

https://doi.org/10.1021/acsomega.2c04448
ACS Omega 2022, 7, 44743−44749

T_{cir}, the location of the amplitude $T_{-+} = 0$ with $S_1 = 141$ nm and $\Delta y = 26$ nm is the EP, which is also demonstrated in the section of eigenvalues and eigenstates. This means that LCP incident light is preserved through the metasurface, with no conversion to RCP. While from the phase of point view, the complete 2π-phase accumulation around the EP can be obtained through any closed path in the parameter space, which is owing to the topological protection in the complex value space.[36] Based on the geometric symmetry, for T_{+-}, it does not possess any point of satisfying $T_{+-} = 0$, and then no complete 2π-phase accumulation occurs, as shown in Figure 4b. Only if the reversal of the "E" structure is in the horizontal or vertical direction, $T_{+-} = 0$.

In the following, we exploited the property of 2π-phase accumulation encircling EP to generate phase-only holograms. A dolphin was chosen as the target image, and it is sampled with 100 pixels × 100 pixels (Figure 5a). The phase distribution of the target image was carried out by the Gerchberg−Saxton algorithm, which contains many cycles of the Fourier transform iterative process (Figure 5b). After that, based on T_{-+} in Figure 4a, each phase pixel was precisely mapped to the "E" structure that justly encircles the EP in the parameter space, delicately corresponding to the desired phase while maintaining a uniform amplitude. The final metasurface that realizes the dolphin hologram is shown in Figure 5c. Compared with the finite number of phase-variation steps in holography, our study accurately characterized each discrete phase, which improves diffraction efficiency and image fidelity. Under LCP incidence, the holographic image could clearly be shown at $\lambda = 550$ nm by FDTD simulations, which fully and completely reproduces the target dolphin (Figure 5d). The other transmission matrix element T_{+-} does not possess EP in the parameter space, and its phase ranges very narrowly and does not cover 2π, so no holographic image could be formed under RCP incidence. Considering the chirality of the "E" structure, we verified that if $\Delta y > 0$, an EP is generated in the T_{-+} transmission spectrum, and the 2π-phase accumulation holds for the LCP. On the contrary, if $\Delta y < 0$, the EP does occur at T_{-+} and 2π-phase variation is responded to RCP. Therefore, polarization multiplexing holography can be realized by utilizing the chirality of "E". Combining two sets of holograms operating with different incident helicities on the same metasurface is the key step to achieve multiplexing holography. As shown in Figure 6a−c, in a unit cell containing two "E" structures, one is $\Delta y > 0$, corresponding to EP at $T_{-+} = 0$, and the other is $\Delta y < 0$, corresponding to EP at $T_{+-} = 0$. First, the discrete phase distributions of two images were generated using the GS algorithm, assuming that the pattern illuminated by LCP is "dolphin1" and the other is "dolphin2" (Figure 6d,e). Then, the two target phase profiles were encoded onto the metasurface, corresponding to the chiral responses of "E" structures in a unit cell. On the illumination of LCP, the metasurface reconstructed "dolphin1" in the holographic image (Figure 6f); conversely, "dolphin2" was presented under RCP (Figure 6g).

3. CONCLUSIONS

In summary, we have demonstrated that a high-index Si dielectric metasurface can be well described by a non-Hermitian open system, where the eigenvalues and eigenstates of the transmission matrix can coalesce into an EP with varying geometrical parameters. The occurrence of EP is ascribed to adjusting the electric and magnetic dipolar resonances with respect to each other within the metasurface. By choosing appropriate metasurface unit structures to encircle the EP in the parameter space, we can obtain a topologically protected full 2π phase in any closed path. As the phase can be completely controlled over the 2π range in each unit cell of the dielectric metasurface by varying parameters, high-resolution computer-generated holography can be realized. Our work combined a dielectric metasurface with a non-Hermitian system, exploiting the nontrivial properties to provide a broader platform for nanophotonics applications.

AUTHOR INFORMATION

Corresponding Authors

Feng Lin − *State Key Lab for Mesoscopic Physics, School of Physics, Peking University, Beijing 100871, China;* orcid.org/0000-0001-8941-7010; Email: linf@pku.edu.cn

Zheyu Fang − *State Key Lab for Mesoscopic Physics, School of Physics, Peking University, Beijing 100871, China; Center for Nanoscale Science and Technology, Academy for Advanced Interdisciplinary Studies, Peking University, Beijing 100871, China; Collaborative Innovation Center of Quantum Matter, Beijing 100871, China;* orcid.org/0000-0001-5780-0728; Email: Zhyfang@pku.edu.cn

Authors

Xiangrong Wu − *State Key Lab for Mesoscopic Physics, School of Physics, Peking University, Beijing 100871, China*

Jiaxi Zhu − *State Key Lab for Mesoscopic Physics, School of Physics, Peking University, Beijing 100871, China*

Xing Zhu − *State Key Lab for Mesoscopic Physics, School of Physics, Peking University, Beijing 100871, China; National Center for Nanoscience and Technology, Beijing 100190, China*

Complete contact information is available at: https://pubs.acs.org/10.1021/acsomega.2c04448

Funding

This work was supported by the National Key Research and Development Program of China (2017YFA0205700, 2015CB932403, and 2017YFA0206000) and the National Science Foundation of China (21790364, 11374023, 61422501, 11674012, 61176120, 61378059, 6097701, and 61521004).

Notes

The authors declare no competing financial interest.

REFERENCES

(1) Yu, N.; Genevet, P.; Kats, M. A.; Aieta, F.; Tetienne, J.-P.; Capasso, F.; Gaburro, Z. Light Propagation with Phase Discontinuities: Generalized Laws of Reflection and Refraction. *Science* **2011**, *334*, 333−337.

(2) Lin, D.; Fan, P.; Hasman, E.; Brongersma, M. L. Dielectric gradient metasurface optical elements. *Science* **2014**, *345*, 298−302.

(3) Wu, C.; Arju, N.; Kelp, G.; Fan, J. A.; Dominguez, J.; Gonzales, E.; Tutuc, E.; Brener, I.; Shvets, G. Spectrally selective chiral silicon metasurfaces based on infrared Fano resonances. *Nat. Commun.* **2014**, *5*, No. 3892.

(4) Chen, H. T.; Taylor, A. J.; Yu, N. A review of metasurfaces: physics and applications. *Rep. Prog. Phys.* **2016**, *79*, No. 076401.

(5) Zhang, F.; Xie, X.; Pu, M.; Guo, Y.; Ma, X.; Li, X.; Luo, J.; He, Q.; Yu, H.; Luo, X. Multistate Switching of Photonic Angular Momentum Coupling in Phase-Change Metadevices. *Adv. Mater.* **2020**, *32*, No. 1908194.

(6) Yuan, Y.; Sun, S.; Chen, Y.; Zhang, K.; Ding, X.; Ratni, B.; Wu, Q.; Burokur, S. N.; Qiu, C. W. A Fully Phase-Modulated Metasurface as An

https://doi.org/10.1021/acsomega.2c04448
ACS Omega 2022, 7, 44743−44749

Energy-Controllable Circular Polarization Router. *Adv. Sci.* **2020**, *7*, No. 2001437.
(7) Zhang, K.; Wang, Y.; Burokur, S. N.; Wu, Q. Generating Dual-Polarized Vortex Beam by Detour Phase: From Phase Gradient Metasurfaces to Metagratings. *IEEE Trans. Microwave Theory Tech.* **2022**, *70*, 200−209.
(8) Ni, X.; Kildishev, A. V.; Shalaev, V. M. Metasurface holograms for visible light. *Nat. Commun.* **2013**, *4*, No. 2807.
(9) Wen, D.; Yue, F.; Li, G.; Zheng, G.; Chan, K.; Chen, S.; Chen, M.; Li, K. F.; Wong, P. W.; Cheah, K. W.; et al. Helicity multiplexed broadband metasurface holograms. *Nat. Commun.* **2015**, *6*, No. 8241.
(10) Khorasaninejad, M.; Ambrosio, A.; Kanhaiya, P.; Capasso, F. Broadband and chiral binary dielectric meta-holograms. *Sci. Adv.* **2016**, *2*, No. e1501258u.
(11) Huang, L.; Zhang, S.; Zentgraf, T. Metasurface holography: from fundamentals to applications. *Nanophotonics* **2018**, *7*, 1169−1190.
(12) Jiang, Q.; Cao, L.; Huang, L.; He, Z.; Jin, G. A complex-amplitude hologram using an ultra-thin dielectric metasurface. *Nanoscale* **2020**, *12*, 24162−24168.
(13) Zhao, Y.; Alu, A. Tailoring the dispersion of plasmonic nanorods to realize broadband optical meta-waveplates. *Nano Lett.* **2013**, *13*, 1086−1091.
(14) Hu, J.; Zhao, X.; Lin, Y.; Zhu, A.; Zhu, X.; Guo, P.; Cao, B.; Wang, C. All-dielectric metasurface circular dichroism waveplate. *Sci. Rep.* **2017**, *7*, No. 41893.
(15) Zhao, X.; Schalch, J.; Zhang, J.; Seren, H. R.; Duan, G.; Averitt, R. D.; Zhang, X. Electromechanically tunable metasurface transmission waveplate at terahertz frequencies. *Optica* **2018**, *5*, 303−310.
(16) Khorasaninejad, M.; Chen, W. T.; Devlin, R. C.; Oh, J.; Zhu, A. Y.; Capasso, F. Metalenses at visible wavelengths: Diffraction-limited focusing and subwavelength resolution imaging. *Science* **2016**, *352*, 1190−1194.
(17) Khorasaninejad, M.; Capasso, F. Metalenses: Versatile multi-functional photonic components. *Science* **2017**, *358*, No. eaam8100.
(18) Lin, R. J.; Su, V.-C.; Wang, S.; Chen, M. K.; Chung, T. L.; Chen, Y. H.; Kuo, H. Y.; Chen, J.-W.; Chen, J.; Huang, Y.-T.; et al. Achromatic metalens array for full-colour light-field imaging. *Nat. Nanotechnol.* **2019**, *14*, 227−232.
(19) Li, L.; Liu, Z.; Ren, X.; Wang, S.; Su, V.-C.; Chen, M.-K.; Chu, C. H.; Kuo, H. Y.; Liu, B.; Zang, W.; et al. Metalens-array-based high-dimensional and multiphoton quantum source. *Science* **2020**, *368*, 1487−1491.
(20) Dembowski, C.; Graf, H. D.; Harney, H. L.; Heine, A.; Heiss, W. D.; Rehfeld, H.; Richter, A. Experimental observation of the topological structure of exceptional points. *Phys. Rev. Lett.* **2001**, *86*, 787−790.
(21) Heiss, W. D. The physics of exceptional points. *J. Phys. A: Math. Theor.* **2012**, *45*, No. 444016.
(22) Feng, L.; El-Ganainy, R.; Ge, L. Non-Hermitian photonics based on parity−time symmetry. *Nat. Photonics* **2017**, *11*, 752−762.
(23) El-Ganainy, R.; Makris, K. G.; Khajavikhan, M.; Musslimani, Z. H.; Rotter, S.; Christodoulides, D. N. Non-Hermitian physics and PT symmetry. *Nat. Phys.* **2018**, *14*, 11−19.
(24) Miri, M. A.; Alu, A. Exceptional points in optics and photonics. *Science* **2019**, *363*, No. eaar7709.
(25) Özdemir, Ş. K.; Rotter, S.; Nori, F.; Yang, L. Parity-time symmetry and exceptional points in photonics. *Nat. Mater.* **2019**, *18*, 783−798.
(26) Kang, M.; Liu, F.; Li, J. Effective spontaneous PT-symmetry breaking in hybridized metamaterials. *Phys. Rev. A* **2013**, *87*, No. 053824.
(27) Kang, M.; Chen, J.; Chong, Y. D. Chiral exceptional points in metasurfaces. *Phys. Rev. A* **2016**, *94*, No. 033834.
(28) Kang, M.; Zhang, T.; Zhao, B.; Sun, L.; Chen, J. Chirality of exceptional points in bianisotropic metasurfaces. *Opt. Express* **2021**, *29*, 11582−11590.
(29) Yu, J.; Ma, B.; Ouyang, A.; Ghosh, P.; Luo, H.; Pattanayak, A.; Kaur, S.; Qiu, M.; Belov, P.; Li, Q. Dielectric super-absorbing metasurfaces via PT symmetry breaking. *Optica* **2021**, *8*, 1290−1295.
(30) Li, Z.; Cao, G.; Li, C.; Dong, S.; Deng, Y.; Liu, X.; Ho, J. S.; Qiu, C.-W. Non-Hermitian Electromagnetic Metasurfaces at Exceptional Points. *Prog. Electromagn. Res.* **2021**, *171*, 1−20.
(31) Lawrence, M.; Xu, N.; Zhang, X.; Cong, L.; Han, J.; Zhang, W.; Zhang, S. Manifestation of PT symmetry breaking in polarization space with terahertz metasurfaces. *Phys. Rev. Lett.* **2014**, *113*, No. 093901.
(32) Hassan, A. U.; Zhen, B.; Soljacic, M.; Khajavikhan, M.; Christodoulides, D. N. Dynamically Encircling Exceptional Points: Exact Evolution and Polarization State Conversion. *Phys. Rev. Lett.* **2017**, *118*, No. 093002.
(33) Gorlach, M. A.; Ni, X.; Smirnova, D. A.; Korobkin, D.; Zhirihin, D.; Slobozhanyuk, A. P.; Belov, P. A.; Alu, A.; Khanikaev, A. B. Far-field probing of leaky topological states in all-dielectric metasurfaces. *Nat. Commun.* **2018**, *9*, No. 909.
(34) Park, S. H.; Lee, S.-G.; Baek, S.; Ha, T.; Lee, S.; Min, B.; Zhang, S.; Lawrence, M.; Kim, T.-T. Observation of an exceptional point in a non-Hermitian metasurface. *Nanophotonics* **2020**, *9*, 1031−1039.
(35) Yang, F.; Prasad, C. S.; Li, W.; Lach, R.; Everitt, H. O.; Naik, G. V. Non-Hermitian metasurface with non-trivial topology. *Nanophotonics* **2022**, *11*, 1159−1165.
(36) Song, Q.; Odeh, M.; Zuniga-Perez, J.; Kante, B.; Genevet, P. Plasmonic topological metasurface by encircling an exceptional point. *Science* **2021**, *373*, 1133−1137.
(37) Guo, A.; Salamo, G. J.; Duchesne, D.; Morandotti, R.; Volatier-Ravat, M.; Aimez, V.; Siviloglou, G. A.; Christodoulides, D. N. Observation of PT-symmetry breaking in complex optical potentials. *Phys. Rev. Lett.* **2009**, *103*, No. 093902.
(38) Lin, Z.; Ramezani, H.; Eichelkraut, T.; Kottos, T.; Cao, H.; Christodoulides, D. N. Unidirectional invisibility induced by PT-symmetric periodic structures. *Phys. Rev. Lett.* **2011**, *106*, No. 213901.
(39) Gu, X.; Bai, R.; Zhang, C.; Jin, X. R.; Zhang, Y. Q.; Zhang, S.; Lee, Y. Unidirectional reflectionless propagation in a non-ideal parity-time metasurface based on far field coupling. *Opt. Express* **2017**, *25*, 11778−11787.
(40) Dong, S.; Hu, G.; Wang, Q.; Jia, Y.; Zhang, Q.; Cao, G.; Wang, J.; Chen, S.; Fan, D.; Jiang, W.; et al. Loss-Assisted Metasurface at an Exceptional Point. *ACS Photonics* **2020**, *7*, 3321−3327.
(41) Huang, Y.; Shen, Y.; Min, C.; Fan, S.; Veronis, G. Unidirectional reflectionless light propagation at exceptional points. *Nanophotonics* **2017**, *6*, 977−996.
(42) Makris, K. G.; El-Ganainy, R.; Christodoulides, D. N.; Musslimani, Z. H. Beam dynamics in PT symmetric optical lattices. *Phys. Rev. Lett.* **2008**, *100*, No. 103904.
(43) Rüter, C. E.; Makris, K. G.; El-Ganainy, R.; Christodoulides, D. N.; Segev, M.; Kip, D. Observation of parity−time symmetry in optics. *Nat. Phys.* **2010**, *6*, 192−195.
(44) Palik, E. D.*Handbook of Optical Constants of Solids*; Academic Press, 1985.
(45) Staude, I.; Miroshnichenko, A. E.; Decker, M.; Fofang, N. T.; Liu, S.; Gonzales, E.; Dominguez, J.; Luk, T. S.; Neshev, D. N.; Brener, I.; Kivshar, Y. Tailoring Directional Scattering through Magnetic and Electric Resonances in Subwavelength Silicon Nanodisks. *ACS Nano* **2013**, *7*, 7824−7832.